

Effect of complex fault geometry and slip style on near-fault strong motions and static displacement

Ryou Honda* and Kiyoshi Yomogida

Division of Earth and Planetary Sciences, Graduate School of Science, Hokkaido University, North 10 West 8, Kita-ku, Sapporo 060-0810, Japan

(Received April 11, 2002; Revised September 8, 2003; Accepted September 19, 2003)

Although there are many studies that deal with complex slip distribution or rupture propagation on an earthquake fault, they usually regard a fault system as a fault of simple geometry. Actual fault systems have highly heterogeneous slip distribution and very complicated shapes, as is often observed through field surveys of surface breaks. In this study, we synthesize seismograms including static displacement near a fault using the discrete wavenumber method in order to estimate the effects of the above types of fault complexity in a quantitative manner. We introduce a complex slip distribution based on the Nojima Fault associated with the 1995 Hyogo-ken Nanbu earthquake. As a result, we show that strong motions at a frequency of lower than 1.0 Hz are strongly affected by the complexity of the fault geometry, at a scale of not more than several km, rather than the rupture propagation style. Distributions of static displacement fluctuate, depending on the fault geometry characterized by the length of each fault segment. Such small-scale variations in fault geometry (≤ 1 km) have been mostly ignored prior to this work. Our results also suggest that details of fault segmentation and bending can be determined by dense observations (e.g., GPS or geological surveys) of static displacement near a fault system, indicating the importance of simultaneous studies on static and dynamic near-fault motions.

Key words: Near field, strong motion, fault geometry, kinematic model.

1. Introduction

High-frequency strong motions recorded near a fault greatly depend on the variability or complexity of rupture velocity and slip distribution on the fault. Synthesized seismograms obtained from a simple Haskell model show good agreement with observed data in the low-frequency range, but it is still very difficult to explain observed high-frequency waves, such as those in a frequency range higher than 1 Hz, in a deterministic manner. To reproduce a spectrum of seismic body-waves (e.g., the ω -square model) at high frequency, several studies have introduced kinematic stochastic models (e.g., Herrero and Bernard, 1994; Bernard *et al.*, 1996; Hisada, 2000) considering various rupture velocities and slip distributions on a fault.

On the other hand, we can often obtain a relatively precise slip distribution, having a resolution of less than 1 km, at the surface by a field survey around an earthquake or active fault system. For example, Nakata *et al.* (1990) surveyed surface fault breaks that appeared during the Philippine Earthquake ($M_s = 7.8$) on July 16, 1990 and estimated its source time function from the slip distribution along the fault. Nakata and Yomogida (1995) obtained the slip distribution along the Nojima Fault that broke during the Hyogo-ken Nanbu earthquake on January 17, 1995. These studies showed the existence of segmented subfaults with crack-like slip distribution

along active fault systems.

Many studies have currently reproduced coseismic rupture processes using inversion techniques (e.g., Hartzell and Heaton, 1986; Kakehi and Irikura, 1996; Yoshida *et al.*, 1996). Slip distribution, rupture velocity, and some other source parameters are obtained accurately by such studies, but complex slip distributions whose scale is less than 1 km, inherent to the generation of waves of a frequency higher than several Hz, are generally not considered in the inversion of rupture processes. In addition, these studies have adopted quite simple fault geometry compared with actual fault systems (e.g., Yeats *et al.*, 1997). Some studies with dynamic fault models have clarified the effects of complex fault geometry such as dip and fault orientations (e.g., Oglesby *et al.*, 2000; Aochi and Fukuyama, 2002). Harris and Day (1993, 1999) computed rupture propagations on parallel strike-slip faults with 2-D and 3-D models. They showed that rupture can be triggered on a separated segment if two segments are overlapped. Aochi *et al.* (2002) showed that if two fault segments are disconnected from each other, rupture at one segment cannot jump into the other in some cases.

Fault segmentation is commonly observed in earthquakes. For example, Li *et al.* (1994) showed the representative size of fault segments (in the 1992 Landers Earthquake) as being several tens of kilometers and found that this feature should exist underground as well as on the surface. Referring to the slip distribution of the Nojima Fault reported by Nakata and Yomogida (1995), we consider a complex but realistic slip distribution in a deterministic manner and calculate near-field seismograms radiating from a fault system in the frequency range of as high as 2.0 Hz. We study a

*Present address: National Research Institute for Earth Science and Disaster Prevention, 3-1 Tennodai, Tsukuba, Ibaraki 305-0006, Japan.

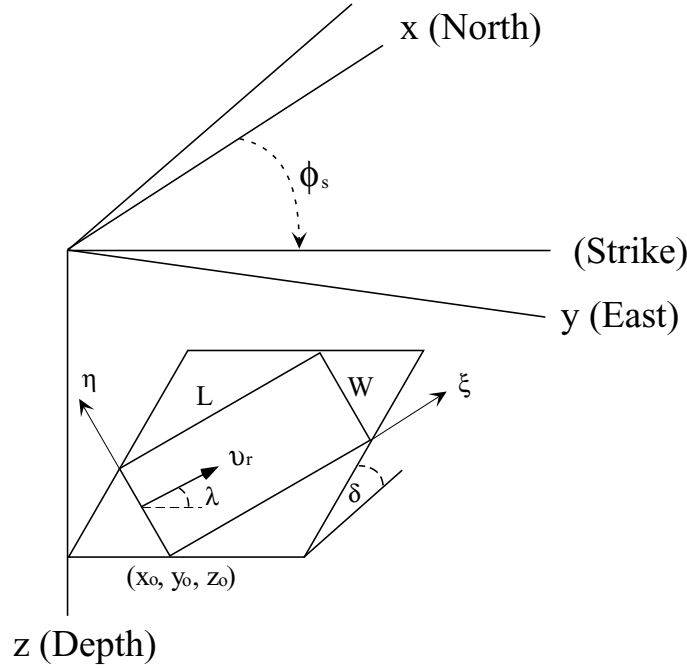


Fig. 1. Fault geometry. L , W , ϕ_s , δ , and λ represent the length, width, strike, dip, and rake of the fault, respectively. The definitions are after Aki and Richards (1980).

pattern of strong motions near the fault system in terms of such complexity of slip distribution, together with its frequency dependency. Another new attempt in this study is to compare static and dynamic near-fault displacements for complex fault models.

2. Method and Models

We synthesize seismograms using the discrete wavenumber method (Bouchon and Aki, 1977), because it can easily introduce a finite fault with complex geometry. In addition, this method can accurately calculate not only dynamic waves such as P- and S-waves but also static displacement with certain criteria on numerical parameters. For example, we introduce a new special potential in order to represent vertically propagating S-waves. The effects of this potential on static displacement are critical in some fault geometries (Honda and Yomogida, 2003a; Honda and Yomogida, 2003b). Plane wave formulations for P-, SV-, and SH-wave potentials radiating from a finite fault are as follows:

$$\phi = \frac{iD}{2L_x L_y k_\beta^2} A I_L I_W \cdot \exp i(k_x(x - x_o) + k_y(y - y_o) - v(z - z_o)), \quad (1)$$

$$\psi_{SV} = \frac{iD}{2L_x L_y k_\beta^2} B_{sv} I_L I_W \cdot \exp i(k_x(x - x_o) + k_y(y - y_o) - \gamma(z - z_o)), \quad (2)$$

$$\psi_{SH} = \frac{iD}{2L_x L_y k_r^2} B_{sh} I_L I_W \cdot \exp i(k_x(x - x_o) + k_y(y - y_o) - \gamma(z - z_o)), \quad (3)$$

where

$$A = -\frac{k_x^2}{v} M_{xx} - \frac{2k_x k_y}{v} M_{xy}$$

$$+2k_x M_{xz} - \frac{k_y^2}{v} M_{yy} + 2k_y M_{yz} - v M_{zz},$$

$$B_{sv} = -\frac{k_x^2}{k_r} M_{xx} - \frac{2k_x k_y}{k_r} M_{xy} + \frac{k_x(k_\beta^2 - 2k_r^2)}{\gamma k_r} M_{xz}$$

$$- \frac{k_y^2}{k_r} M_{yy} + \frac{k_y(k_\beta^2 - 2k_r^2)}{\gamma k_r} M_{yz} + k_r M_{zz},$$

$$B_{sh} = -\frac{k_x k_y}{\gamma} M_{xx} + \frac{k_x^2 - k_y^2}{\gamma} M_{xy}$$

$$+ k_y M_{xz} + \frac{k_x k_y}{\gamma} M_{yy} - k_x M_{yz},$$

with moment tensors related to fault geometry (see box 4.4 of Aki and Richards, 1980), and

$$I_L \equiv \frac{\exp iL(\omega/v_r - C_{12}k_x - C_{22}k_y \pm C_{32}\Lambda) - 1}{(\omega/v_r - C_{12}k_x - C_{22}k_y \pm C_{32}\Lambda)i}, \quad (4)$$

$$I_W \equiv \frac{\exp iW(-C_{11}k_x - C_{21}k_y \pm C_{31}\Lambda) - 1}{(-C_{11}k_x - C_{21}k_y \pm C_{31}\Lambda)i}, \quad (5)$$

$k_r = \sqrt{k_x^2 + k_y^2}$ are the horizontal wavenumbers, and k_α and k_β are the P- and S-wave wavenumbers. After analytical integration of the point sources distributed over a rectangular fault, we obtain the above finiteness terms, I_L and I_W . Λ is the vertical wavenumber (i.e., $v = \sqrt{k_\alpha^2 - k_r^2}$ for P-waves or $\gamma = \sqrt{k_\beta^2 - k_r^2}$ for S-waves; $\text{Im}v, \text{Im}\gamma \leq 0$). D , L , and W are the slip, length, and width of the fault, respectively. As shown in Fig. 1, we assume a unilateral and unidirectional rupture propagation. ξ represents the direction of rupture propagation and η the other direction of the fault segment (see Chin, 1992). The transformation matrix of the coordinate systems in Eqs. (4) and (5) is

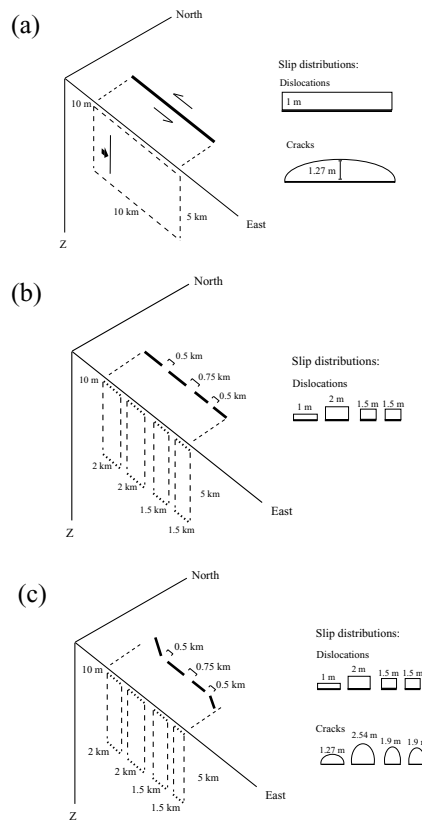


Fig. 2. Configurations of (a) single left-lateral fault, (b) segmented fault, and (c) Nojima Fault models. Rupture propagates unidirectionally from west to east. Slip distributions on a fault plane are illustrated at right. In the case of step dislocations, the slip at each point follows a step function and its amount is constant in each fault segment, while the dynamic source factor (Bouchon, 1978) is used as a slip function in the case of shear cracks.

$$\begin{pmatrix} C_{11} & C_{12} \\ C_{21} & C_{22} \\ C_{31} & C_{32} \end{pmatrix} = \begin{pmatrix} \sin \phi_s \cos \delta \cos \lambda - \cos \phi_s \sin \lambda & \sin \phi_s \cos \delta \sin \lambda + \cos \phi_s \cos \lambda \\ -\cos \phi_s \cos \delta \cos \lambda - \sin \lambda \sin \phi_s & -\cos \phi_s \cos \delta \sin \lambda + \sin \phi_s \cos \lambda \\ -\sin \delta \cos \lambda & -\sin \delta \sin \lambda \end{pmatrix}.$$

where ϕ_s , λ , and δ represent strike, rake, and dip angles, respectively.

Using the above formulations, we next calculate and compare the maximum velocity distributions for several fault models to estimate the effects of kilometer-scale complexity of fault geometry and slip distribution. We compare fault models varying (1) the fault geometry and (2) the rupture style; that is, the temporal and spatial function of slips over a fault or each subfault. Three vertical strike-slip fault models with a step dislocation in time are examined: a single-fault model, segmented model, and Nojima Fault model. These geometries and slip distributions are shown in Fig. 2. All the models have a common rupture velocity (2.4 km/s) and total moment release. The depth of the fault top is 10 m. Slip distributions are illustrated at the right of each model with the identification of "Dislocations." The segmented model and the Nojima Fault model consist of four segments, and correspond to the fault geometry surveyed by Nakata and Yomogida (1995), as shown in Fig. 3. The amount of slip in each segment is constant to approximate the corresponding average amount of slips. The segments of the Nojima Fault model are not aligned in a straight manner.

One may argue that fault breaks at the surface do not re-

flect the main features of underground fault geometry. Although some previous studies have supported the hypothesis that segmentations of several kilometers in size should exist under the ground (e.g., Li *et al.*, 1994), it is necessary to check the validity of the use of information on surface fault breaks, as shown in Fig. 3, for seismic studies controlled mainly by subsurface fault slips. Figure 4 shows a fractal analysis of the surface fault geometry of the Nojima Fault in Fig. 3 (Hayashi, 1996). Following the procedure of Okubo and Aki (1987), the total length L of the fault system is measured by filling it with circles of radius r . If the fault system shows a self-similar character, the total length L follows a power of r , and its fractal dimension D is defined as $L \propto r^{1-D}$.

It is clear that two types of self-similarity are observed: $\log L = 4.02 + 0.04 \log r$ for a scale of less than 40 m, and $\log L = 4.14 - 0.03 \log r$ for an equal or longer scale. Their fractal dimensions are 0.96 ± 0.03 and 1.03 ± 0.02 , respectively. Fractal dimensions of major fault systems in Japan are similar to the latter value at a scale of down to several hundred meters (Matsumoto *et al.*, 1992). That is, a surface fault trace of larger than several hundred meters appears to provide the overall character of major faults in Japan. At a smaller scale, the complex surface breaks of the Nojima Fault result in a clearly different fractal dimension of larger than 1. The effect of surface soft layers should modify the actual fault character of the overall subsurface fault geometry. In contrast, the fault character revealed at the larger scale in the above fractal analysis is likely to reflect

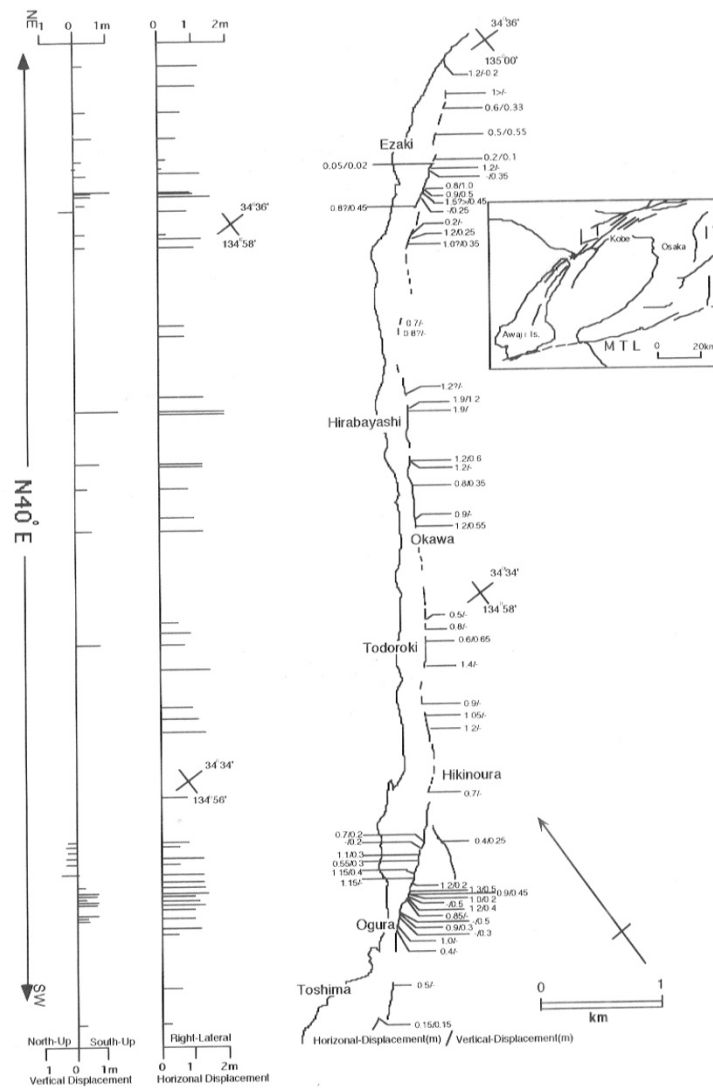


Fig. 3. Surface fault ruptures associated with the 1995 Hyogo-ken Nanbu earthquake. The fault trace is not straight, and the distributions of horizontal displacement show a crack-like shape (after figure 2 of Nakata and Yomogida (1995)).

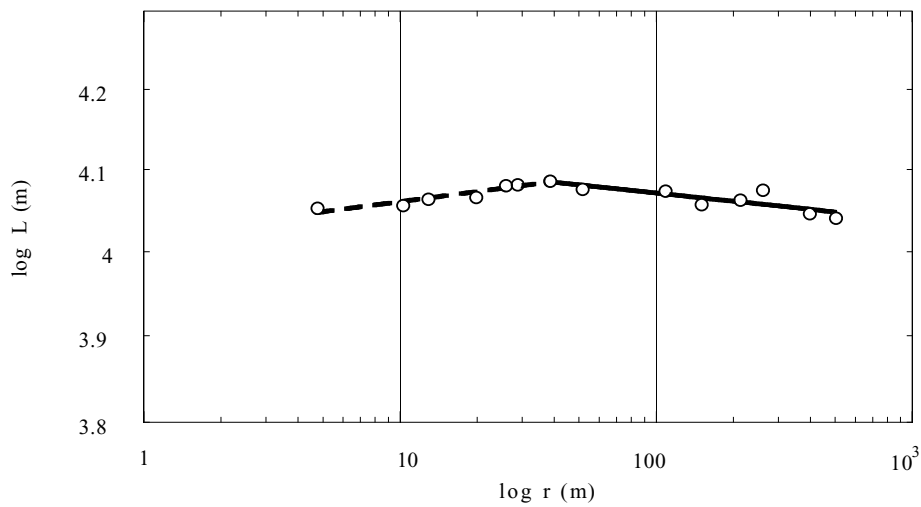


Fig. 4. Logarithmic relationship between the total length of fault segments L and the measured scale length r for the Nojima Fault (Hayashi, 1996). The fractal dimensions are 1.03 ± 0.02 for $r < 40$ m and 0.96 ± 0.03 for $r \geq 40$ m, respectively.

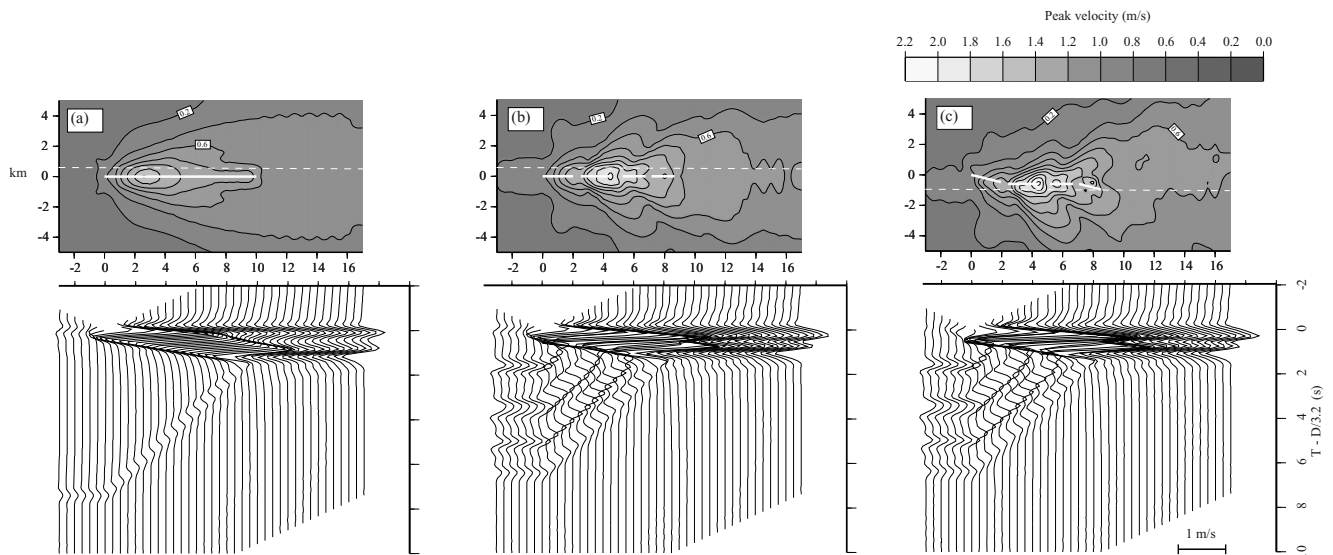


Fig. 5. Peak velocities distributions and synthetic wave-forms of fault-normal-component in the frequency range of 0.1–2.0 Hz for (a) the single-fault model, (b) the segmented model, and (c) the Nojima Fault model. The fat white lines represent the surface projections of the fault, and the dotted white lines show the locations of observers of the waveforms.

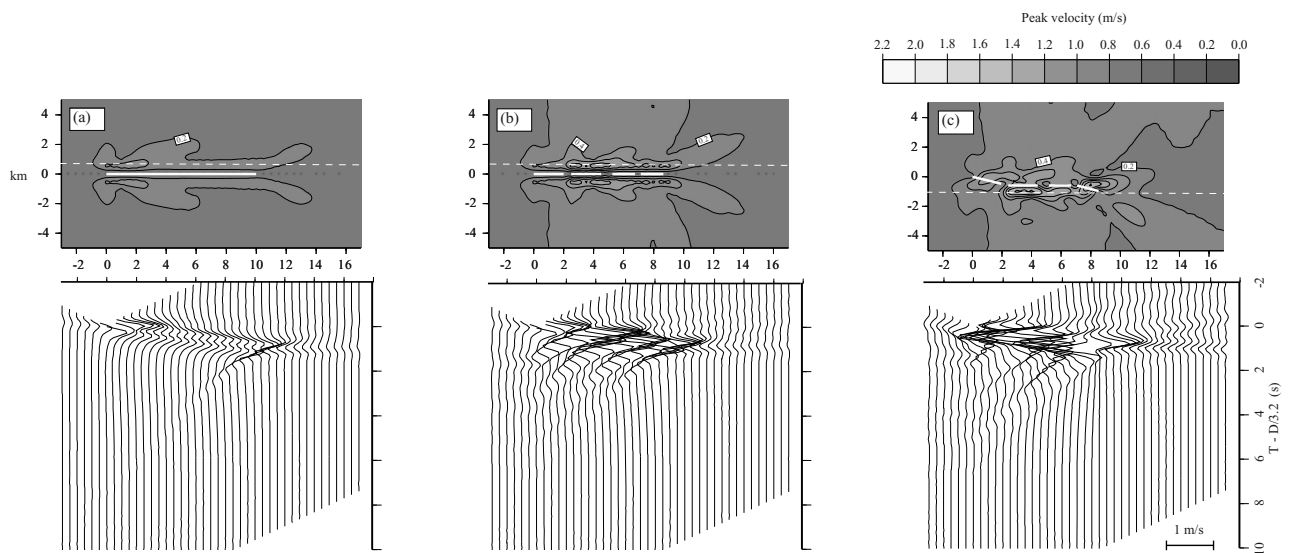


Fig. 6. Same as Fig. 5 for the fault-parallel component.

the overall subsurface fault geometry.

The above result supports the hypothesis that fault breaks at the surface do not significantly differ from those under the ground at a scale of 40 meters or more, for the Nojima Fault. It should be noted that our main goal in the present study is not to pursue the actual features of rupture propagation in the Nojima Fault during the 1995 Hyogo-ken Nanbu earthquake, but to demonstrate a complex distribution of near-fault ground motions for a segmented fault, compared with a fault of rather simple geometry, using kinematic source models.

3. Effect of Fault Geometry and Slip Distribution

Let us first take the “Dislocations” model (Fig. 2) as a rupture style, assuming the slip at each point as being a step in time, in order to focus on the effect of fault geometry. Figures 5 to 7 show peak velocity distributions and waveforms

in the frequency range of 0.1–2.0 Hz for (a) the single-fault model, (b) the segmented model, and (c) the Nojima Fault model, respectively. These peak velocities are taken for the normal, parallel, and vertical components independently. For all three components, the most conspicuous phase that generates the peak velocity at each observation point is related to the nearby passage of the rupture front. This phase is mainly composed of near-field S-waves. Its apparent propagation velocity is 2.4 km/s, corresponding to the rupture velocity.

In the single-fault model, the largest velocity in all three components is located near the rupture initiation point, so we can refer to it as the starting phase. Regions of high velocity extend in the direction of rupture propagation, due to the well-known directivity effect. The fault-parallel and vertical component velocities are nearly one-half or one-third the velocity of the fault-normal component.

The fault-parallel and vertical component velocities in the

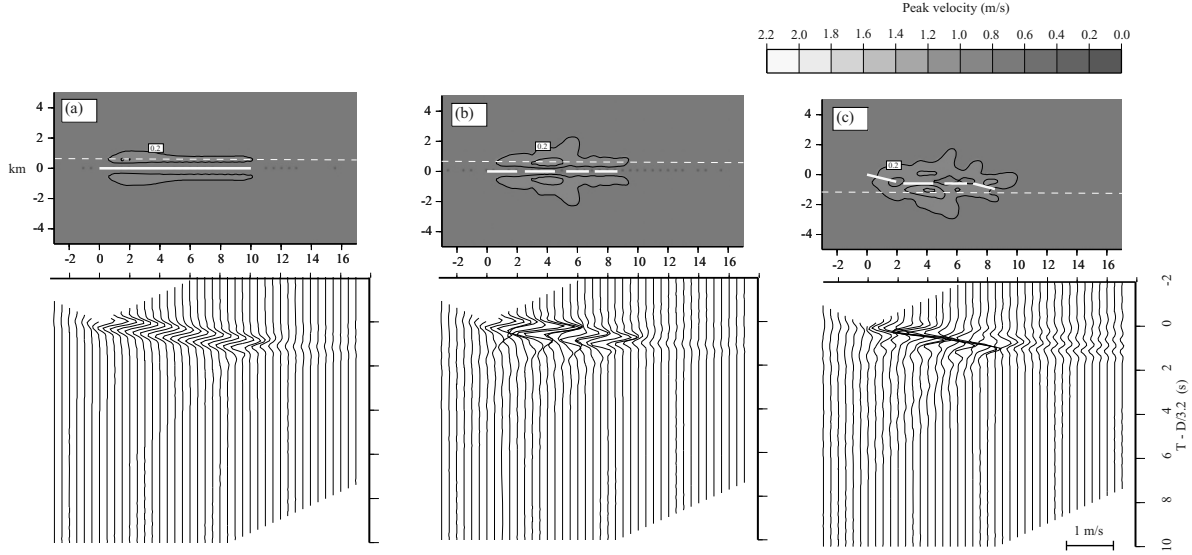


Fig. 7. Same as Fig. 5 for the vertical component.

segmented model (b in Figs. 5 to 7) are higher than in the single fault model even with the same total moment release. This effect is due to the strong starting and stopping phases of rupture at each fault segment.

In the Nojima Fault model, on the other hand, all three component velocities show complex patterns, compared with the other two models. There is a particularly noticeable difference in the fault-parallel component (Fig. 6(c)). Areas of high velocity are observed as small spots on and between fault segments, as seen in Fig. 6(c), due to the combined effect of the stopping phase and near-field S-waves related to the nearby passage of the rupture front. The bending of fault traces is effective in amplifying ground velocities because large fault-normal components are observed in this case. The vertical component velocity (Fig. 7(c)) shows a similar pattern to the other cases.

4. Effect of Rupture Style

The temporal variation of slip at a given point on the fault was assumed to be a step function in the previous examples. Referring to Bouchon (1978), we now introduce a 2-D crack-like model whose final slip distribution is shown in Fig. 2 with the identification of “Cracks”. The recent rapid progress in research on the dynamic rupture process should be taken into account fully, but the present kinematic model gives very similar near-fault ground motions to such dynamic cases, as confirmed later (see Section 5.3). Previous geophysical and geographical studies have suggested that this crack-like rupture model can explain observed near-field displacement seismograms well in some cases (e.g., Archuleta and Hartzell, 1981; Yomogida, 1988; Ruppert and Yomogida, 1992). Final slip distributions at the surface also support this type of slip model (e.g., Yeats *et al.*, 1997). We next compare ground velocity distributions for the step dislocation model, as described in the previous section, with those for the crack-like model in order to understand the importance of the rupture style, using the same fault geometries.

Here let us briefly explain numerical formulations for the crack-like rupture model (Fig. 8), following Bouchon (1978).

Bouchon (1978) defined an approximate slip function for two-dimensional shear cracks, as follows:

$$D(\xi, t) = \begin{cases} \frac{2D(L/2, \infty)}{L} \sqrt{\xi(v_r t - \xi)} H(t - \xi/v_r), & 0 \leq t \leq L/v_r \\ \frac{2D(L/2, \infty)}{L} \sqrt{\xi(L - \xi)}, & t \geq L/v_r \end{cases} \quad (6)$$

where v_r denotes the rupture velocity and $D(L/2, \infty)$ is the final slip in the middle of the crack. ξ and L were previously defined in Fig. 1. Equation (6) represents a semi-ellipse that grows linearly with time until the rupture stops at the other end of the crack. Since $D(\xi, t)$ is distributed in $0 \leq \xi \leq v_r t$ ($\leq L$), we approximate it by a broken line with $(M + 1)$ points (Fig. 8). The slip at ξ is given by

$$D(\xi, t) = \begin{cases} a_m \xi + b_m v_r t & \text{for } \frac{m-1}{M} v_r t < \xi < \frac{m}{M} v_r t \\ 0 & \text{for } \xi > v_r t, \end{cases} \quad 0 \leq t \leq L/v_r, \quad (7)$$

$$D(\xi, t) = a_m \xi + b_m L \quad \text{for } (m-1)\Delta L < \xi < m\Delta L, \quad t \geq L/v_r, \quad (8)$$

where

$$a_m = \frac{D(m\Delta L, \infty) - D[(m-1)\Delta L, \infty]}{\Delta L},$$

$$b_m = m \frac{D[(m-1)\Delta L, \infty]}{L} - (m-1) \frac{D(m\Delta L, \infty)}{L},$$

$$\Delta L = L/M,$$

and

$$D(\xi, \infty) = \frac{2D(L/2, \infty)}{L} \sqrt{\xi(L - \xi)}. \quad (9)$$

The Fourier transform of the slip function is given by

$$D(\xi, \omega) = \int_{-\infty}^{\infty} D(\xi, t) e^{-i\omega t} dt.$$

The dynamic source factor $S(\omega)$ is defined by

$$S(\omega) = \sum_{m=1}^M \int_{(m-1)\Delta L}^{m\Delta L} D(\xi, \omega) e^{i\beta\xi} d\xi, \quad (10)$$

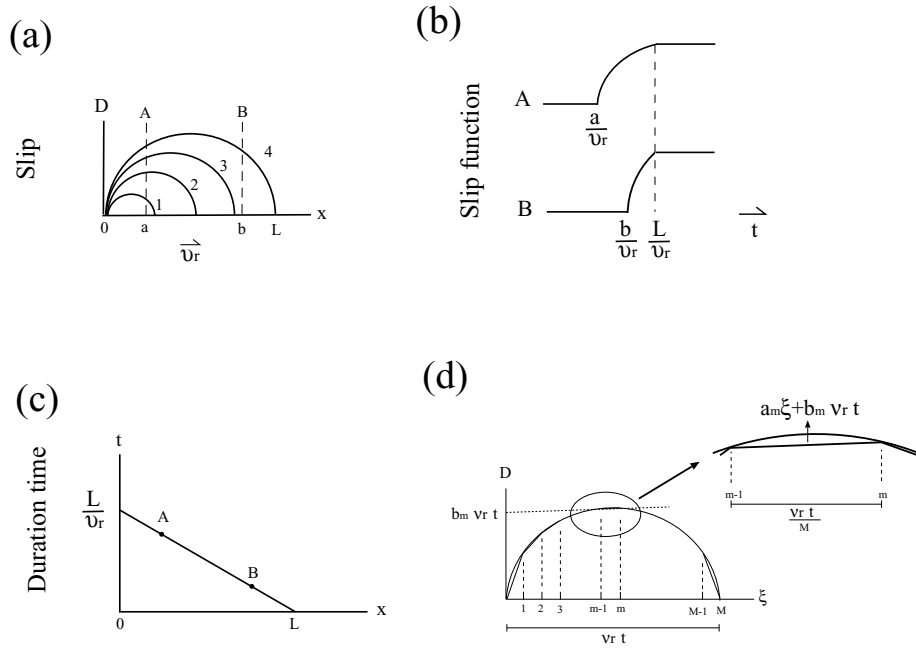


Fig. 8. Schematic illustrations of the crack model used in this study, showing (a) slips as a function of distance x along the fault from the nucleation point ($x = 0$) at each time of $L/4v_r$, (b) slip time functions at points A and B, (c) spatial variation of duration times on the fault as a function of distance, and (d) a semi-ellipse, divided in M arcs, at time t . Each arc is represented by a line that has a slope a_m and intersects the D-axis at $b_m v_r t$. Parameter v_r is the rupture velocity.

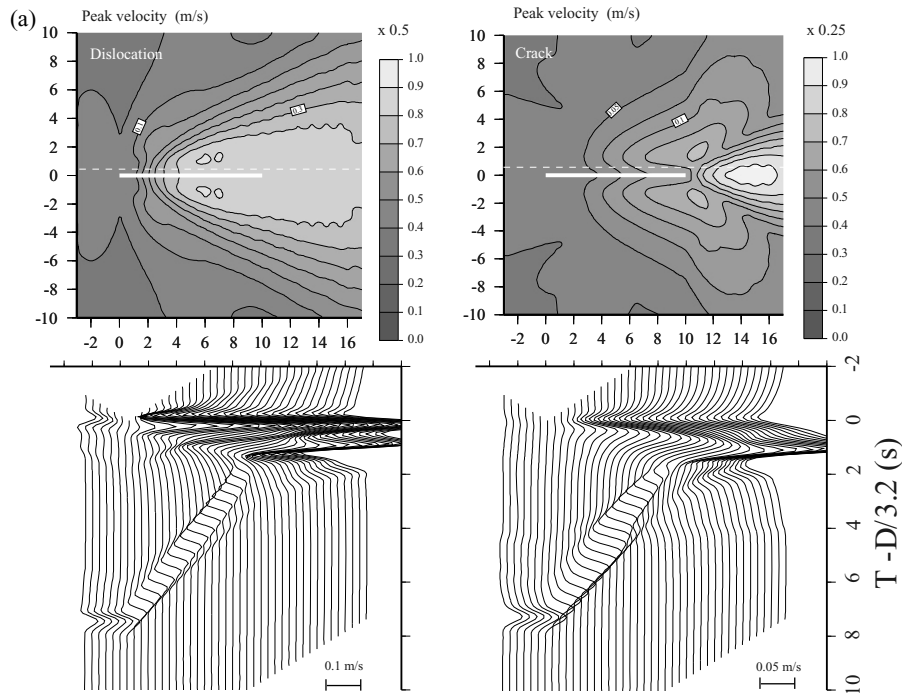


Fig. 9. Comparison of distributions and waveforms of (a) fault-normal, (b) fault-parallel, and (c) vertical component peak velocities in the dislocation model and the crack-like model. The fat and dotted white lines are the same as those in Fig. 5. The scale of waveform amplitude in the crack-like model is twice that in the dislocation model. The origin time of each waveform is reduced by the S-wave velocity. The thin dotted lines in the waveforms of (b) correspond to the stopping phase that reaches the observers at the same time.

with $\beta = (-C_{12}k_x - C_{22}k_y \pm C_{32}\Delta)$ expressing the entire rupture process. The above two-dimensional crack-like model can be obtained only by replacing I_L in Eq. (4) by $S(\omega)$. Hereafter, we call the model with a step function as the “dislocation model” and that with $S(\omega)$ as the “crack-like model.”

Figure 9 compares the peak velocity distributions and velocity waveforms of the dislocation and crack-like models with a single straight fault whose top is buried in at a depth of 1 km. In the dislocation model, large velocity values are observed along the fault in all the components with a strong phase, which is related to the nearby passage of the rupture

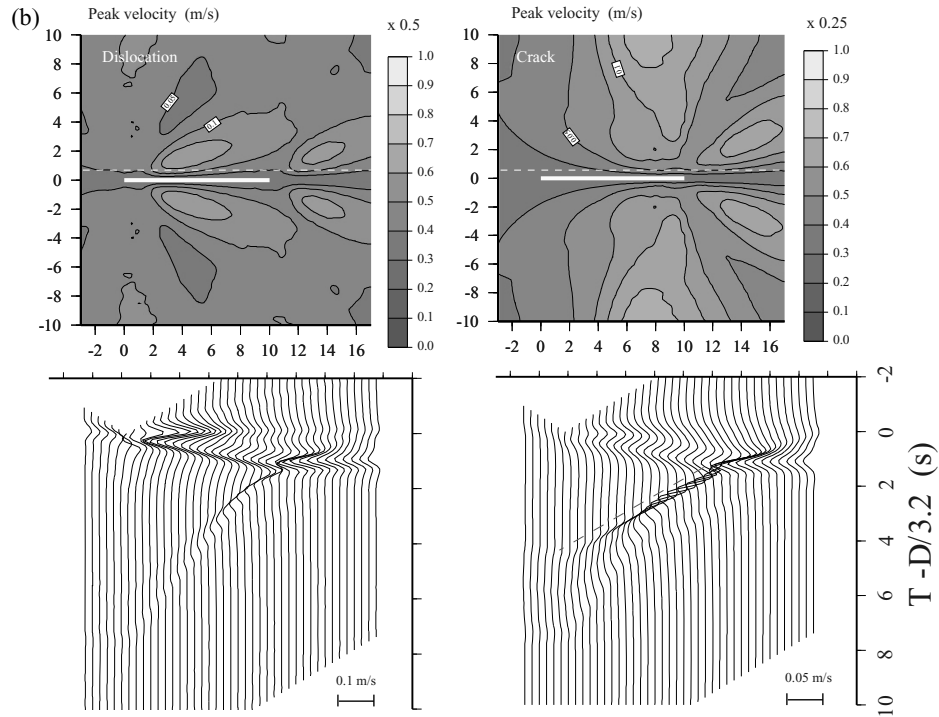


Fig. 9. (continued).

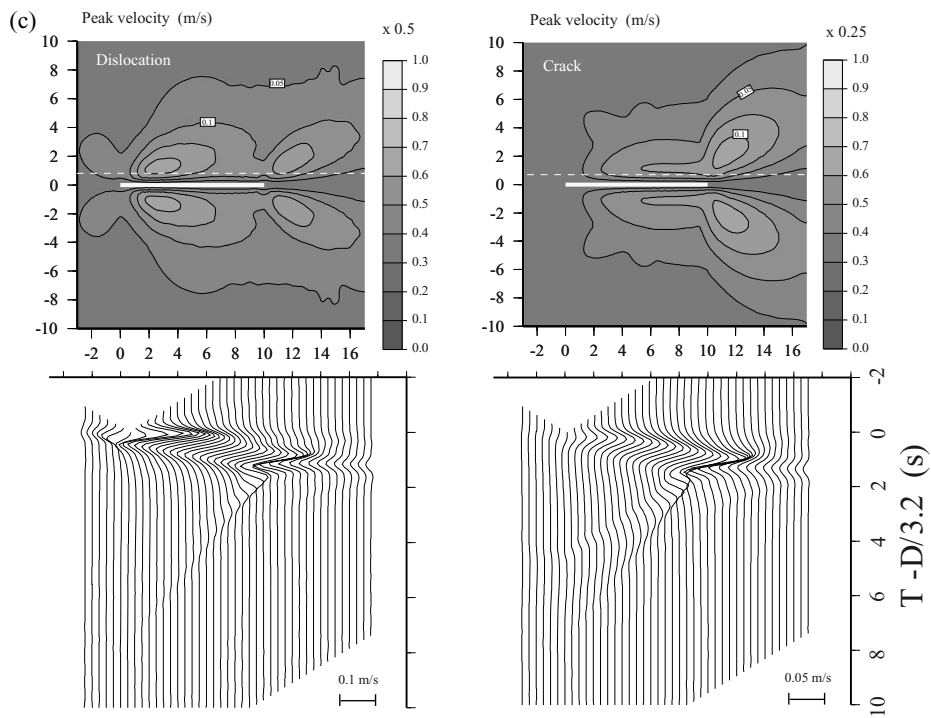


Fig. 9. (continued).

front. Strong velocities are observed only around a rupture stopping point (i.e., at one end of the fault) in the crack-like model. This result is caused by the small slip rate in most of the fault plane except near the stopping point, as illustrated in Fig. 8(a).

On the other hand, a very strong phase not observed in the dislocation model appears clearly in the fault-parallel component (the thin dotted line in Fig. 9(b)). Since the slip at

each fault point terminates simultaneously, corresponding to the stopping time of the rupture, the so-called stopping phase is radiated from every point on the fault plane. This is an artifact due to 2-D modeling, and we shall construct a more realistic 3-D crack-like model in the next section. As far as the maximum ground velocity distribution is concerned, the existence of this phase does not alter our results significantly, as shown later.

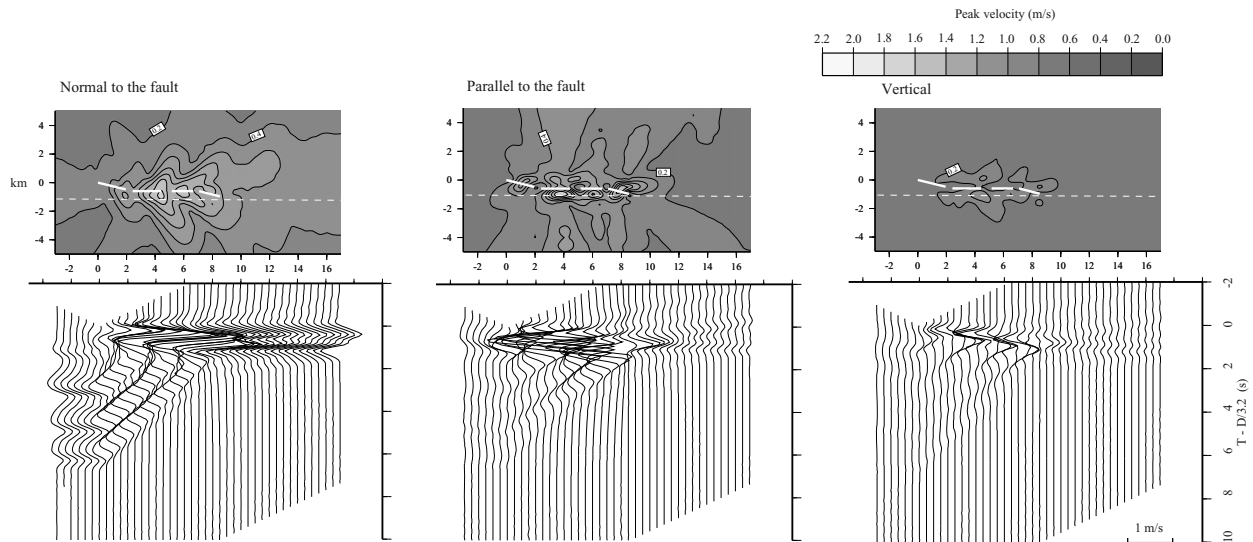


Fig. 10 Same as Figs. 5(c), 6(c), and 7(c) for the crack-like model.

Next, we apply the above crack-like slip distribution to the Nojima Fault model (Fig. 2(c)) to estimate more realistic peak velocity distributions for this earthquake. The obtained peak velocity distributions are shown in Fig. 10 compared with (c) in Figs. 5 to 7 for the previous dislocation model (i.e., temporal slip as a step function). The peak velocity of the fault-parallel component becomes larger (~ 1.6 m/s) than that of the dislocation model (~ 1.3 m/s) (Fig. 6(c)), and larger than the fault-normal component, that is dominant in the dislocation model (Fig. 5(c)). Very strong motions only near the fault in the fault-normal component were reported for this earthquake; for example, the “damage belt” and “characteristic velocity pulses” observed in Kobe (Kawase, 2000). Complex superposition of refracted and direct waves caused such phenomena in Kobe. Our results show that complex fault geometry and crack-like propagation can cause such a complex strong motion distribution pattern. Similarly to the present result for the Nojima Fault, the very complex fault geometry of the underground fault system in Kobe should be responsible for such strong motions. Although detailed waveform inversions have already spotted several local areas on the fault system radiating large seismic energy (e.g., Sekiguchi *et al.*, 1996; Kakehi and Irikura, 1996), the above result clearly shows that velocity distribution can be easily modified by even small changes in fault segmentation and bending as well as rupture style. It is necessary to take these factors into consideration when we try to retrieve more details of the fault process.

5. Frequency-Dependent Characteristics

Generally speaking, the overall slip distribution and rupture propagation pattern can be obtained by waveform inversion in the frequency range of lower than 1.0 Hz. In order to understand the frequency dependence of the velocity distribution near a fault, we apply band-pass filters to the synthetic seismograms obtained in the previous sections. Peak velocity distributions in three frequency ranges (0.1–1.0 Hz, 1.0–2.0 Hz, and 2.0–4.0 Hz) are shown in Figs. 11 to 13. First, we compare these results among the three fault-

geometry models, that is, the single-fault, segmented, and Nojima Fault models using the dislocation model (i.e., slip as a step). Next, we compare the difference between the dislocation and crack-like models with the Nojima Fault model, which we hereafter refer to as the first and second Nojima Fault models, respectively.

5.1 Comparison among dislocation models

In the frequency range of lower than 2.0 Hz, the distributions of fault-normal component peak velocities (on the left in Figs. 11 and 12) are not largely affected by the fault geometry (i.e., bending or segmentation) except for their absolute values. The largest amplitude appears grossly in the middle of the fault in each case. This component includes the major phase corresponding to the nearby passage of the rupture front. In contrast, the distributions of the other two components (i.e., the fault-parallel and vertical components) are strongly affected by the fault geometry even in the low-frequency range (Fig. 11). The more complex the fault geometry becomes, the larger the velocities observed in these two components. For example, a region of large amplitude (~ 1.2 m/s, as much as the largest value of the fault-normal component) is observed near the second segment of the fault system in the Nojima Fault model, which consists of the stopping phase generated in the end of the first segment and the nearby passage of the rupture front.

As the frequency increases (Fig. 13), the distributions become quite different in all the components, particularly between the single-fault model and the others. Very strong fault-normal velocities (~ 2.8 m/s) are observed in a large region extending in the direction of the rupture propagation in the other two models, because of the directivity effect. Velocity spectra in the frequency domain in such a region have a peak around 2.0 Hz, and this frequency is defined by the length of the fault segments and rupture velocity (see, for example, section 14.1.5. of Aki and Richards (1980)). As a result, the ground velocity distributions are quite different between the frequencies that are lower (Figs. 11 and 12) and higher (Fig. 13) than this frequency.

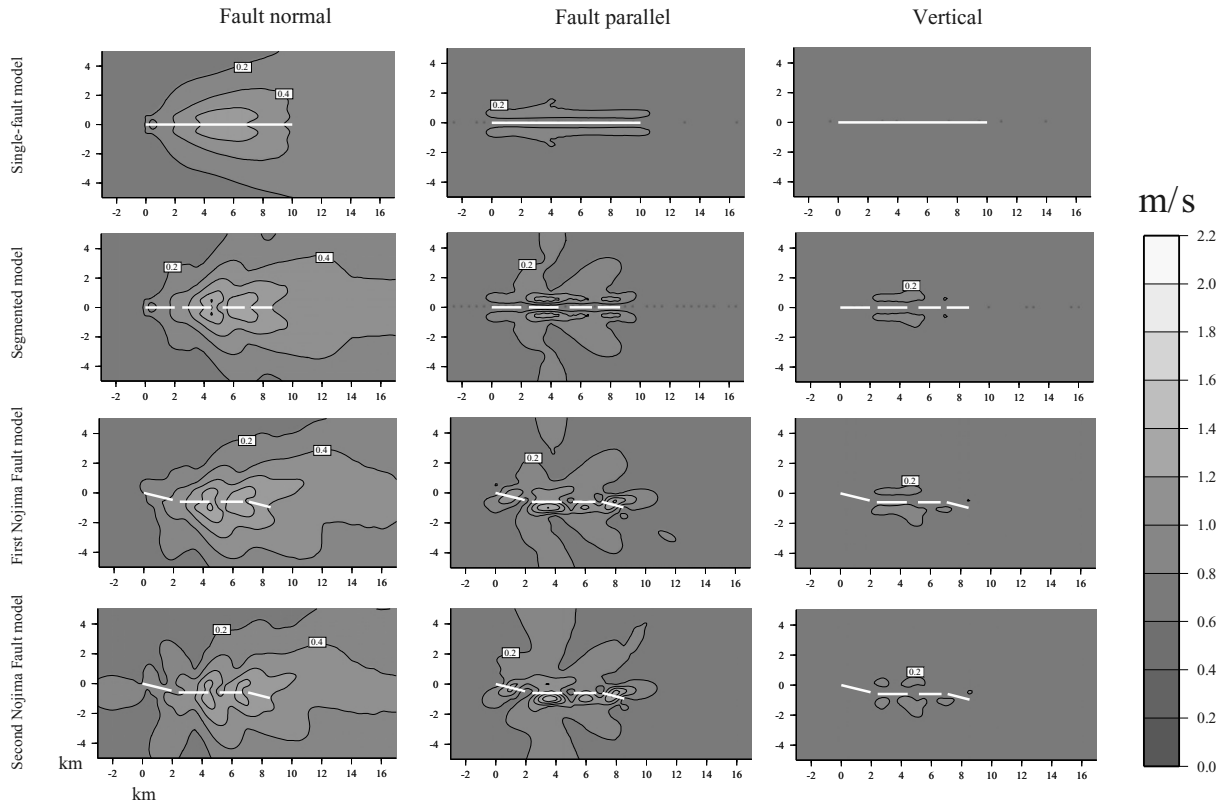


Fig. 11. Filtered peak velocity distributions for all models. The frequency range is 0.1–1.0 Hz.

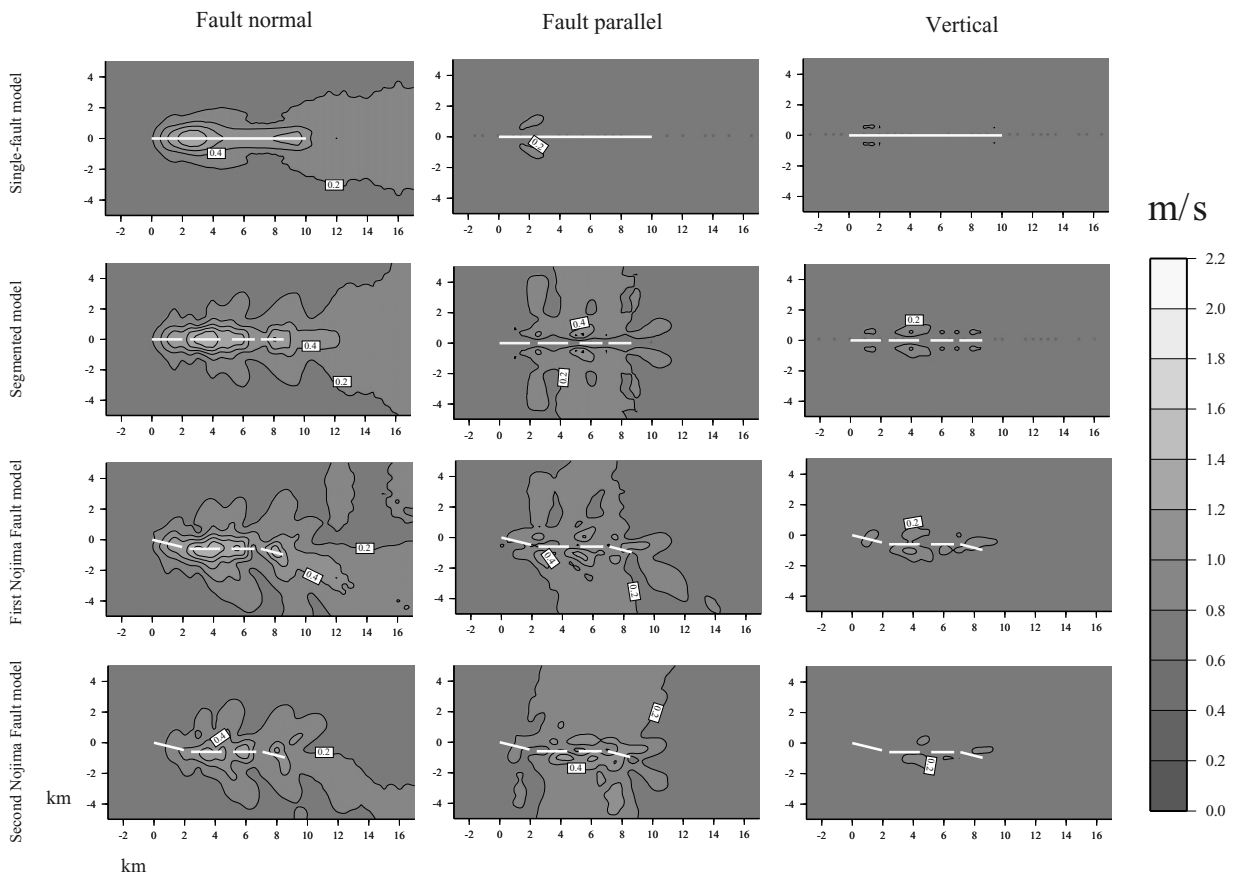


Fig. 12. Same as Fig. 11 for the frequency range of 1.0–2.0 Hz.

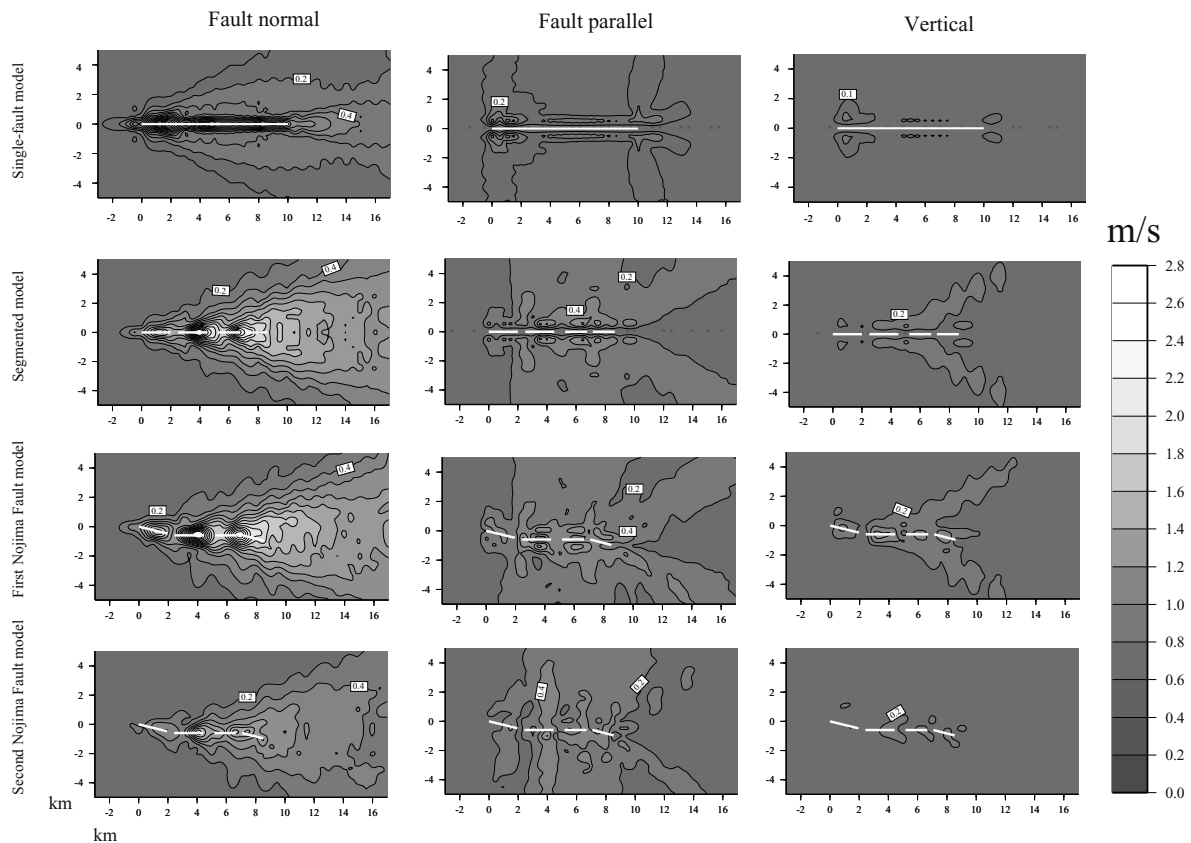


Fig. 13. Same as Fig. 11 for the frequency range of 2.0–4.0 Hz.

5.2 Comparison between dislocation and crack-like models

Next, we compare ground velocity distributions for two slip styles, that is, between the first and the second (crack-like slip) Nojima Fault models as shown in the lower two figures of Figs. 11 to 13. In the frequency range of lower than 2.0 Hz (Figs. 11 and 12), there is little difference in ground velocity distribution, although the absolute values are slightly smaller in the second model.

Figure 14 shows a comparison of the waveforms of these two models in the same frequency range as Fig. 11; that is, 0.1–1.0 Hz. Although the distributions of peak velocities, which are largely controlled by high-frequency waves, are similar (Fig. 11), their waveforms are quite different even in such a low-frequency range because of the different spatial and temporal slip distributions (Aki and Richards, 1980; Yomogida, 1988). This is because near-field terms of relatively low frequency are dominant and different between the two slip models. In other words, the slip style has less effect than the fault geometry on peak ground velocity distribution in the low-frequency range in spite of the waveforms themselves are rather different.

Since smooth rupture propagation in the second Nojima Fault model excites fewer high-frequency seismic waves, the distribution in the high-frequency range shows much smaller amplitude than in the first model (Fig. 13). The dominant feature of the velocity spectra in the second model is a peak around 1.0 Hz from the slip duration time determined by the segment length (1–2 km) and rupture velocity (2.4 km/s). In

the second model, high-frequency seismic waves are generated only around the termination point of the rupture at each segment, and the pattern does not show a conspicuous feature of directivity as in the model of simple fault geometry (the top of Fig. 13).

5.3 Comparison between 2-D and 3-D crack-like models

The crack-like model used above has some unrealistic features of rupture propagation; for example, as shown in Fig. 9(b). Here, we introduce a more realistic 3-D rupture model in order to confirm the effect of such artifacts on our results, particularly on near-fault ground velocity distribution. The configuration of the new model is shown in Fig. 15. We divide each segment into 3×5 subfaults that have various amounts of slip. The total seismic moment is same as in the 2-D crack-like model. The rupture is initiated at the left end of the first segment (the asterisk in Fig. 15) and propagates circularly with a constant velocity of 2.4 km/s. Each point starts slipping when the rupture front reaches that point and stops at the arrival of a healing front propagating backwards at S-wave velocity (Archuleta and Hartzell, 1981). This rupture model is purely kinematic, but it gives a very similar spatial-temporal distribution of slips to that of a single fault segment or a block of the entire fault system, based on recent dynamic rupture propagation models, including laboratory-based friction laws (e.g., Fukuyama and Madariaga, 1998; Inoue and Miyatake, 1998; Miyatake, 2000). Note that the length of one fault segment in Fig. 15 is about 2 km, while the dynamic rupture processes referring to any observations

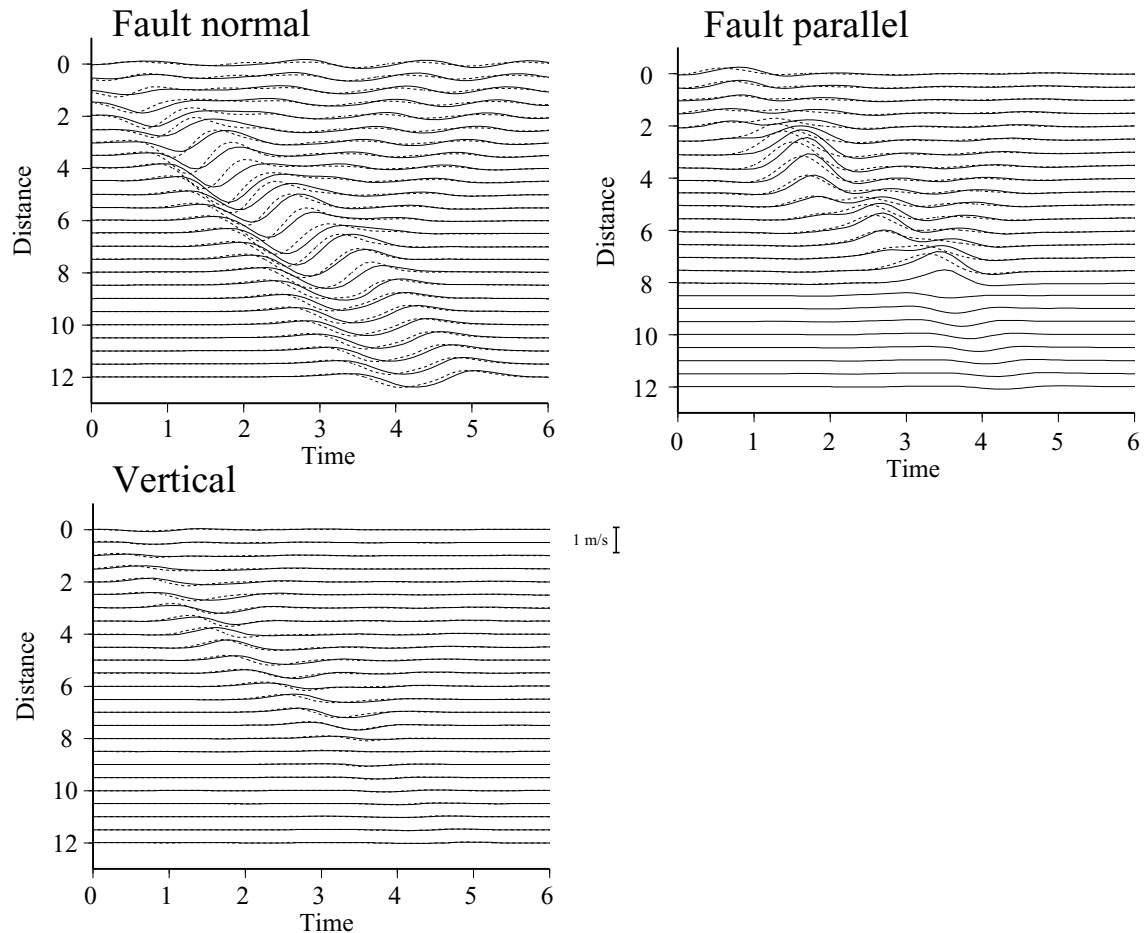


Fig. 14. Velocity waveforms of the first (dotted lines) and the second (solid lines) Nojima Fault models in the frequency range of 0.1–1.0 Hz. Observers are located 500 m away from the fault along the fault strike (same as Fig. 10 except for the number of observers).

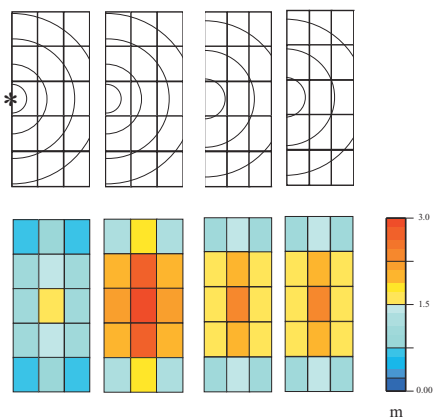


Fig. 15. Configuration of a more realistic 3-D fault model. Top: Schematic representation of rupture propagation. The rupture starts at the center of the first segment (represented by the asterisk) and propagates circularly with a constant velocity. Bottom: Final slip distribution in each segment.

in the previous studies exceed 5 km or more. Only numerical studies have adopted a dynamic rupture of a smaller scale than the present one.

Figure 16 shows maximum ground velocity distributions for a block of the 3-D crack-like model (Fig. 15) in three frequency ranges. These results should be compared with

those for the 2-D crack-like model of the same Nojima Fault geometry (i.e., the second Nojima Fault model) in Fig. 11 (0.1–1.0 Hz), Fig. 12, (1.0–2.0 Hz) and Fig. 13 (2.0–4.0 Hz), as well as Fig. 10 for all the frequency ranges. The overall feature (e.g., large amplitude in the fault-normal and the fault-parallel components amplified in a narrow region) is similar to that in the previous 2-D crack-like model except for some minor aspects. For example, the fault-parallel component in the range of 1.0–2.0 Hz has a slightly larger amplitude than in the 2-D model (the bottom of Fig. 12). In the realistic 3-D case, the rupture propagates not only in the fault-strike or horizontal direction but also in the down-dip direction. Such an anti-plane rupture propagation generates strong motions in the fault-parallel component (Miyatake, 2000). Fault-parallel motions are dominant around the second and third segments because these segments are shorter than the other segments with dominant anti-plane fault motions at the segment edges, as seen in Fig. 15. In the high-frequency range of 2.0–4.0 Hz, the amplitudes are generally smaller than in the 2-D model (the bottom of Fig. 13), particularly in the fault-parallel component, because the slip at each point stops not simultaneously but gradually as the healing phase propagates backwards. This result confirms that our use of the 2-D crack-like model is not problematic, as long as we pay attention to the ground velocity distribution near a fault, compared with dynamic rupture models. This

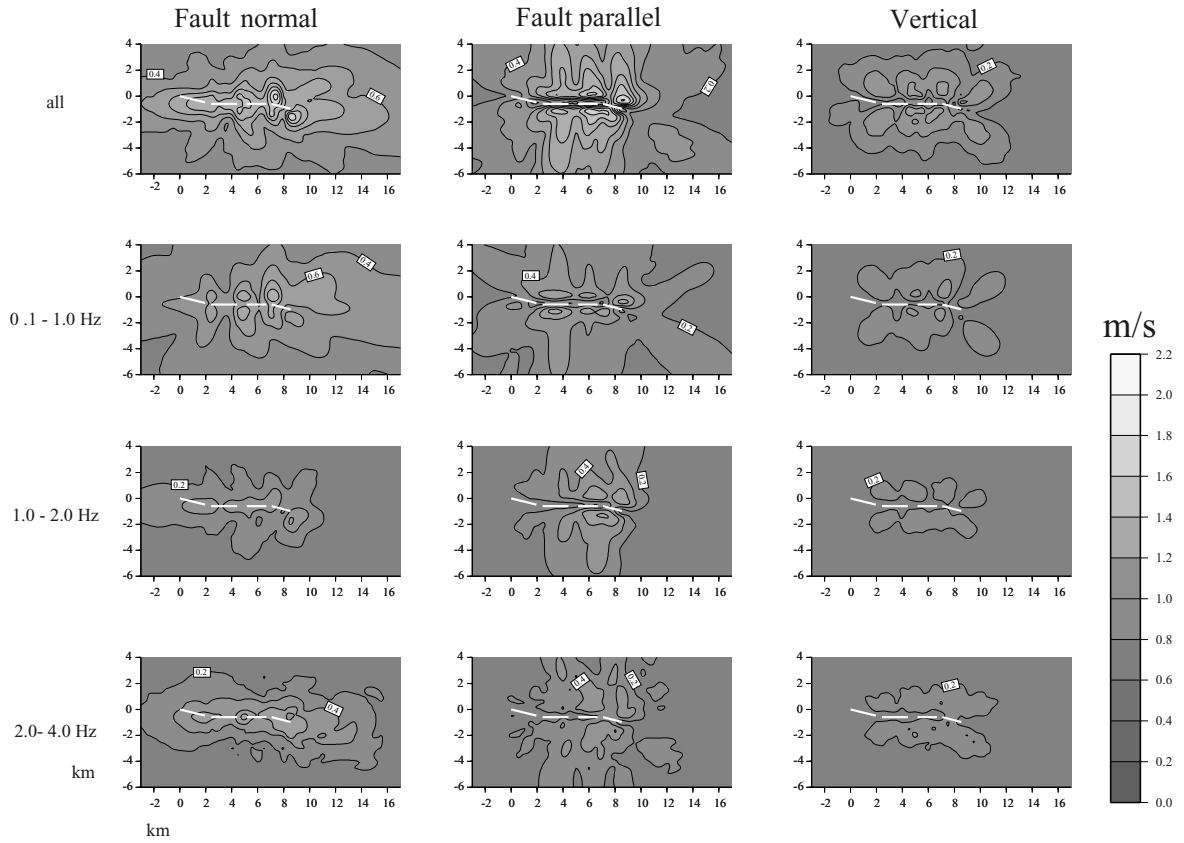


Fig. 16. Maximum ground velocity distributions in the 3-D fault model in various frequency ranges. Note that the amplitudes in the highest frequency range are amplified to three times the original level.

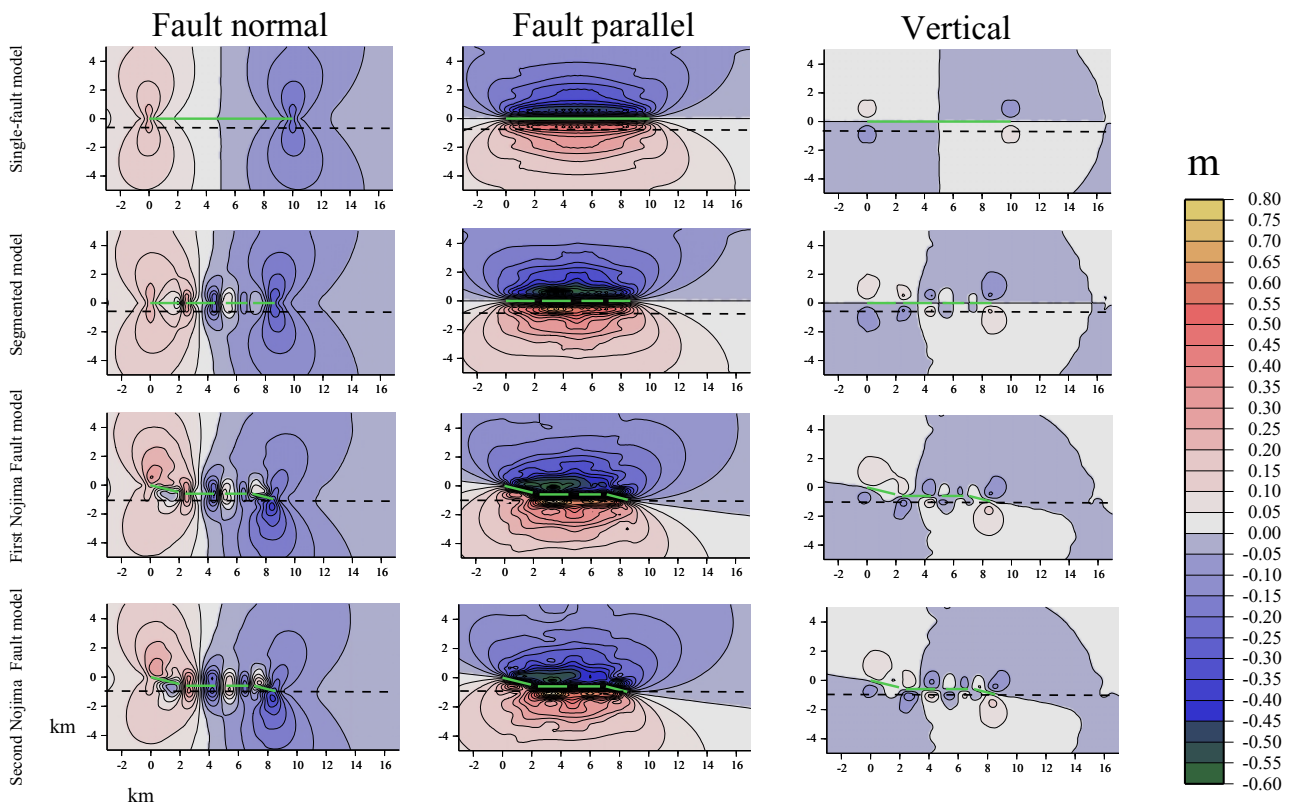


Fig. 17. Static displacement distributions in all models.

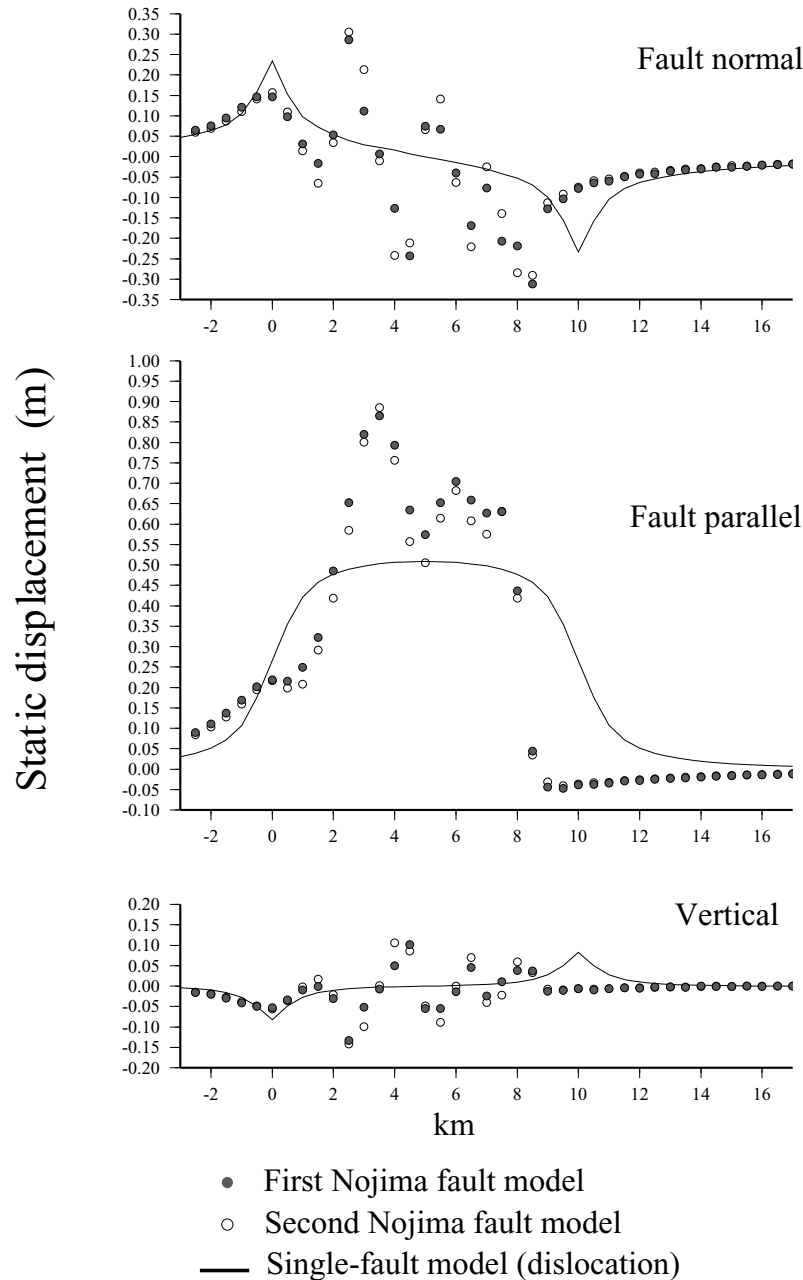


Fig. 18. Cross section of the observers on the dotted lines of Fig. 17.

model appears to generate excessive high-frequency waves over 2 Hz, but we must remember that, as explained in the previous section, the complexity of the fault geometry also becomes effective or important in such a case.

6. Static versus Dynamic Motions

Honda and Yomogida (2003a, b) showed that both dynamic and static displacements around a fault can be precisely computed by the discrete wavenumber method under a certain criterion of the involved parameters. In addition to the frequency dependency discussed in the previous section, we next compare static displacements with the above dynamic motions in the four fault models of Figs. 11 to 13. Figure 17 shows the corresponding distributions of static displacement. The static slip distribution can be readily surveyed after the main shock, so relating the surface displacements

and the rupture process is very important. Joint inversion of both static (i.e., crustal movement) and dynamic motions has been proven to be powerful in imposing strong constraints to the rupture process (e.g., Wald *et al.*, 1996).

The single-fault model gives a static-displacement distribution quite different from the other three models, suggesting that the fault segmentation is an essential factor in the generation of complex patterns in static displacement, although they appear only near the fault system. The fault-parallel component static displacement has the largest amplitude, agreeing with the slip component on the fault, while dynamic motions are usually the largest in the fault-normal component. Spatial variations of static displacement in the present models of complex fault geometry have a characteristic wavelength of 1.5–2 km, which corresponds to the scale of fault segmentation (Fig. 18). Since the static displacements

ment is not affected by the rupture style (i.e., the spatial and temporal distribution of coseismic slips) but only determined by the final slip distribution, the difference between the two Nojima models (the bottom two rows in Fig. 17) is virtually zero. Although we do not show the result here, static displacement is also similar in the realistic 3-D crack-like model introduced in the previous section, for the same reason. The effect of either small fault bending or detailed slip distribution in each segment does not alter the overall pattern of static displacement.

Combining this result with those obtained in the previous sections, it is evident that the feature of fault segmentation is critical, particularly at a low frequency, including static displacements ($\omega = 0$). GPS, In-SAR, and SPOT observations will be helpful in providing accurate data on surface gaps across the fault trace, although other data should be used concurrently because of errors such as the bias of satellite motion (Michel and Avouac, 2002).

7. Conclusions

Both dynamic and static displacements near a fault system were synthesized by the discrete wavenumber method for complex fault geometry and various rupture styles, down to the order of less than a kilometer in a deterministic manner. We first used a fault model with complex geometry that has often been obtained in recent field surveys of active fault systems (e.g., the 1995 Hyogo-ken Nanbu earthquake and the 1999 Chi-Chi earthquake). According to our standpoint that such information on fault systems is very useful in the quantitative estimation of complex near-field ground motions, we introduced our Nojima Fault model as an example of highly segmented faults and demonstrated how complex ground motions can be radiated from segmented fault geometry alone. Compared with a single straight fault, actual faults with segmentation into several subfaults and the fluctuation of segment orientations result in quite variable strong motions near the fault even at a relatively low frequency (0.1–1.0 Hz). For example, ground velocities are weak in the fault-parallel component for a straight strike-slip fault even close to the fault, while this component has a comparable amplitude in the fault-normal component, which is generally large, even with the introduction of a slight bending of fault segments.

Another important factor is how slips expand over a fault plane. If the fault slips in a single-crack manner (i.e., a long source-time duration at the initiation point of the rupture and very short at the stopping point), the stopping phase becomes much stronger than the phase related to the nearby passage of the rupture front, while the rupture-passage phase is the largest in a conventional slip model such as the Haskell-type dislocation model of the constant source-time duration on the fault. For a strike-slip fault, a pulse-like phase in the fault-parallel component is clearly observed only along the fault trace, and the amplitude is the largest where the rupture stops. The fault-normal component is very small on the fault but strong outside of the fault near the stopping point (Fig. 9). These results strongly suggest that we cannot even predict the overall strong motion pattern only by estimating a detailed slip distribution on a fault without knowledge of the rupture style.

In the frequency range of lower than 1.0 Hz, fault-parallel component motions are strongly affected by the effects of fault geometry (i.e., bending and segmentation), but this does not hold true for the fault-normal component. Although the effect of the rupture style on peak velocity distribution is small in this low-frequency range, the waveforms are quite different. While the waveform of the fault-normal component is symmetric before and after the nearby passage of the rupture front in the dislocation model, the crack-like rupture gives an asymmetric waveform due to an asymmetric stress distribution with respect to the rupture front (Aki and Richards, 1980). In actual seismic observations, high-frequency waves are strongly affected by complex propagation path and site effects even if a station is very close to a fault. Near-field terms with relatively low-frequency components, however, have the potential to retrieve the rupture style only by the gross feature of recorded seismograms (e.g., Yomogida, 1988).

In the high-frequency range of 2.0–4.0 Hz, the directivity effect is dominant. Since the corresponding wavelength is less than the scale of each fault segment in this study, stopping phases generated at the edge of each segment become very strong. Smooth rupture propagation in the crack-like model is effective in producing much smaller ground velocities than the dislocation model.

Since our dislocation model and 2-D crack-like model may be criticized as unrealistic, we have introduced a more realistic kinematic fault model that follows recent 3-D dynamic rupture models, including the propagation of a healing phase (Fig. 15). These rupture features are consistent with some recent seismic observations (e.g., Wald and Heaton, 1994; Sekiguchi *et al.*, 2000). The more realistic 3-D kinematic rupture model gives a slightly smaller amplitude at high frequency (≥ 2 Hz) than our 2-D crack-like model, particularly in the fault-normal component (Figs. 13 and 16). Nevertheless, the overall ground velocity distribution, including its amplitude, will not alter if we simulate a realistic dynamic rupture process carefully with the rupture model of Fig. 15.

Since the Hyogo-ken Nanbu earthquake, many studies have attempted to solve the mechanism of the damage belt in Kobe caused by strong fault-normal motions (e.g., Inoue and Miyatake, 1997; Furumura and Koketsu, 1998). Our results, however, suggest that fault systems constructed by segments having a scale of less than 1 km will be able to generate very strong motions in a narrow region around the fault, not only in the fault-normal but also the fault-parallel components.

The majority of current source studies uses a very complex slip distribution over a fault with simple geometry. Although the extent to which segmentations appearing at the surface reflect the underground features should also be discussed, this study emphasizes the importance of fault geometry complexity as well as rupture style (i.e., whether or not the rupture front propagates smoothly over each fault segment in the manner of a single crack-like model) in future studies on strong motions near a fault.

Static displacement is also strongly affected by fault segmentation or overall slip distribution. Since it is determined by the final amount of slip, neither the rupture style nor minor subfault bending is important. We may be able to ob-

tain precise information on the fault segmentation if there are dense observation points (e.g., GPS reference points and control points) around the fault system. After constraining the fault geometry and slip distribution in this manner, we may be truly able to retrieve details of the rupture style; that is, the “dynamic source model” in recent literature (e.g., Beroza and Mikumo, 1996; Cotton and Coutant, 1997; Kase and Kuge, 2001). Since our approach can simultaneously compute static and dynamic motions near a fault system (Honda and Yomogida, 2003b), it will become a powerful tool in future to retrieve complex source processes with GPS as well as near-fault strong motion data composed of both static and dynamic components.

Acknowledgments. We are deeply grateful to Dr. David Oglesby and an anonymous reviewer for their valuable comments on our manuscript.

References

- Aki, K. and P. G. Richards, *Quantitative Seismology: Theory and Methods*, W. H. Freeman and Co., San Francisco, 1980.
- Aochi, H. and E. Fukuyama, Three-dimensional nonplanar simulation of the 1992 Landers earthquake, *J. Geophys. Res.*, **102**, 10.1029/2000JB000061, 2002.
- Aochi, H., R. Madariaga, and E. Fukuyama, Effect of normal stress during rupture propagation along nonplanar faults, *J. Geophys. Res.*, **107**, 10.1029/2001JB000500, 2002.
- Archuleta, R. and S. Hartzell, Effects of fault finiteness on near-source ground motion, *Bull. Seis. Soc. Am.*, **71**, 939–957, 1981.
- Bernard, P., A. Herrero, and C. Berge, Modeling directivity of heterogeneous earthquake ruptures, *Bull. Seis. Soc. Am.*, **86**, 1149–1160, 1996.
- Beroza, G. and T. Mikumo, Short slip duration in dynamic rupture in the presence of heterogeneous fault properties, *J. Geophys. Res.*, **101**, 22,449–22,460, 1996.
- Bouchon, M., A dynamic source model for the San Fernando earthquake, *Bull. Seis. Soc. Am.*, **68**, 1555–1576, 1978.
- Bouchon, M. and K. Aki, Discrete wave-number representation of seismic-source wave fields, *Bull. Seis. Soc. Am.*, **67**, 259–277, 1977.
- Chin, B. H., Simultaneous Study of the Source, Path and Site Effects on Strong Ground Motion during the 1989 Loma Prieta Earthquake, Ph.D. thesis, University of Southern California, 1992.
- Cotton, F. and O. Coutant, Dynamic stress variations due to shear faults in a plane-layered medium, *Geophys. J. Int.*, **128**, 676–688, 1997.
- Fukuyama, E. and R. Madariaga, Rupture dynamics of a planar fault in a 3D elastic medium: Rate- and slip-weakening friction, *Bull. Seis. Soc. Am.*, **88**, 1–17, 1998.
- Furumura, T. and K. Koketsu, Specific distribution of ground motion during the 1995 Kobe earthquake and its generation mechanism, *Geophys. Res. Lett.*, **25**, 785–788, 1998.
- Harris, R. and S. Day, Dynamics of fault interaction: Parallel strike-slip faults, *J. Geophys. Res.*, **98**, 4461–4472, 1993.
- Harris, R. and S. Day, Dynamic 3-D simulations of earthquakes on en echelon faults, *Geophys. Res. Lett.*, **26**, 2089–2092, 1999.
- Hartzell, S. H. and T. H. Heaton, Rupture history of the 1984 Morgan Hill, California, earthquake from the inversion of strong-motion data records, *Bull. Seis. Soc. Am.*, **76**, 649–674, 1986.
- Hayashi, H., Fractal analysis of the fault system and stress drop of aftershocks for Hyogoken-nambu earthquake, Senior Thesis, Hiroshima University, 1996.
- Herrero, A. and P. Bernard, A kinematic self-similar rupture process for earthquakes, *Bull. Seis. Soc. Am.*, **84**, 1216–1228, 1994.
- Hisada, Y., A theoretical omega-square model considering the spatial variation in slip and rupture velocity, *Bull. Seis. Soc. Am.*, **90**, 387–400, 2000.
- Honda, R. and K. Yomogida, Contribution of vertically traveling plane S-waves to dynamic and static displacements near a finite fault, *Geophys. J. Int.*, **152**, 443–454, 2003a.
- Honda, R. and K. Yomogida, Static and dynamic displacement near a fault with the discrete wavenumber method, *Phys. Earth Planet. Inter.*, **137**, 107–127, 2003b.
- Inoue, T. and T. Miyatake, 3-D simulation of near-field strong motion: Basin edge effect derived from rupture directivity, *Geophys. Res. Lett.*, **24**, 905–908, 1997.
- Inoue, T. and T. Miyatake, 3D simulation of near-field strong ground motion based on dynamic modeling, *Bull. Seis. Soc. Am.*, **88**, 1445–1456, 1998.
- Takehi, Y. and K. Irikura, Estimation of high-frequency wave radiation areas on the fault plane by the envelope inversion of acceleration seismograms, *Geophys. J. Int.*, **125**, 892–900, 1996.
- Kase, Y. and K. Kuge, Rupture propagation beyond fault discontinuities: Significance of fault strike and location, *Geophys. J. Int.*, **147**, 330–342, 2001.
- Kawase, H., Strong motion evaluation in the near-fault region considering the slip-velocity function of the source, in *Confronting Urban Earthquakes*, edited by K. Toki, pp. 410–413, 2000.
- Li, Y., K. Aki, D. Adams, and A. Hasemi, Seismic guided waves trapped in the fault zone of the Landers, California, earthquake of 1992, *J. Geophys. Res.*, **99**, 11,705–11,722, 1994.
- Matsumoto, N., K. Yomogida, and S. Honda, Fractal analysis of fault systems in Japan and the Philippines, *Geophys. Res. Lett.*, **19**, 357–360, 1992.
- Michel, R. and J.-P. Avouac, Deformation due to the 17 August 1999 Izmit, Turkey, earthquake measured from SPOT images, *J. Geophys. Res.*, **107**, 10.1029/2000JB000102, 2002.
- Miyatake, T., Computer simulation of strong ground motion near a fault using dynamic fault rupture modeling: Spatial distribution of the peak ground velocity vectors, *Pure Appl. Geophys.*, **157**, 2063–2081, 2000.
- Nakata, T. and K. Yomogida, Surface fault characteristics of the 1995 Hyogoken-nambu earthquake, *J. Natural Disas. Sci.*, **16**, 1–9, 1995.
- Nakata, T., H. Tsutsumi, R. S. Punongbayan, R. E. Rimando, J. Daligdig, and A. Daag, Surface faulting associated with the Philippine earthquake of 1990, *Journal of Geography*, **99**, 95–112, 1990.
- Oglesby, D., R. J. Archuleta, and S. Nielsen, The three-dimensional dynamics of dipping fault, *Bull. Seism. Sci. Am.*, **90**, 616–628, 2000.
- Okubo, P. G. and K. Aki, Fractal geometry in the San Andreas fault system, *J. Geophys. Res.*, **92**, 345–355, 1987.
- Ruppert, S. D. and K. Yomogida, A crack-like rupture model for the 19 September 1985 Michoacan, Mexico, earthquake, *PAGEOPH*, **138**, 407–427, 1992.
- Sekiguchi, H., K. Irikura, T. Iwata, Y. Takehi, and M. Hoshiba, Minute locating of faulting beneath Kobe and the waveform inversion of the source process during the 1995 Hyogo-ken Nanbu, Japan, earthquake using strong ground motion records, *J. Phys. Earth*, **44**, 473–487, 1996.
- Sekiguchi, H., K. Irikura, and T. Iwata, Fault geometry at the rupture termination of the 1995 Hyogo-ken Nanbu earthquake, *Bull. Seis. Soc. Am.*, **90**, 117–133, 2000.
- Wald, D. J. and T. Heaton, Spatial and temporal distribution of slip for the 1992 Landers, California, earthquake, *Bull. Seis. Soc. Am.*, **84**, 668–691, 1994.
- Wald, D. J., T. Heaton, and K. Hudnut, The slip history of the 1994 Northridge, California, earthquake determined from strong-motion, teleseismic, GPS, and leveling data, *Bull. Seis. Soc. Am.*, **86**, S49–S70, 1996.
- Yeats, R. S., K. Sieh, and C. R. Allen, *The Geology of Earthquakes*, Oxford University Press, New York, 1997.
- Yomogida, K., Crack-like rupture processes observed in near-fault strong motion data, *Geophys. Res. Lett.*, **15**, 1223–1226, 1988.
- Yoshida, S., K. Koketsu, B. Shibazaki, T. Sagiya, T. Kato, and Y. Yoshida, Joint inversion of near- and far-field waveforms and geodetic data for the rupture process of the 1995 Kobe earthquake, *J. Phys. Earth*, **44**, 437–454, 1996.